

Title TBC

Louie Corpe

Supervisors: Paul Dauncey, Chris Seez

June 10, 2014

Abstract

An overview of the study of the Higgs boson via its decay to two photons at CMS is presented. A brief introduction into the history of the Standard Model and the motivation for Higgs searches is given, as well as a detailed description of the CMS experiment at CERN. The analysis of the $H \rightarrow \gamma\gamma$ decay mode is described in some detail, with reference to recent work. A discussion on the outlook and future work to be done in this decay channel is also given.

Contents

1	Introduction	2
2	The SM and $H \rightarrow \gamma\gamma$	3
2.1	The Standard Model	3
2.2	$H \rightarrow \gamma\gamma$	3
3	The CMS detector	4
3.1	Overview of the LHC and CMS	4
3.2	The electromagnetic calorimeter (ECAL)	5
3.3	Other subdetectors	6
4	The $H \rightarrow \gamma\gamma$ analysis	7
4.1	Overview of the legacy analysis	7
4.2	Photon resolution studies	8
4.2.1	Motivation	8
4.2.2	Method and Result	8
4.2.3	Estimation of the error	10
4.2.4	Checks	11
5	ECAL clustering validation service work	12
5.1	Overview of the task	12
5.2	The ECALELF tool	12
5.3	CMSSW_7_0_X and CMSSW_5_3_X electron matching	13
5.4	Initial validation work	14
5.4.1	Energy	14
5.4.2	E/p	14
5.4.3	R_9	14
5.4.4	Bremmstrahlung fraction	16
5.4.5	η, ϕ coordinates	16
5.4.6	$Z \rightarrow e^+e^-$ invariant mass	17
5.5	Next Steps	18
6	Future work	18
7	Conclusion	18
	References	18

1 Introduction

The $H \rightarrow \gamma\gamma$ analysis played an important role in the discovery of the Higgs boson in 2012 (CITE FIXME), and has recently published an analysis using all of the data from run I (known as the “legacy analysis”). This analysis has demonstrated the sensitivity of this decay mode: an observation of a Higgs boson signal with over 5σ certainty allowed a standalone discovery to be claimed CITE LEGACY (FIXME - will be published?). My Ph.D. will involve working within this group, and helping run further studies on the Higgs boson’s properties when the LHC starts running again in March 2015. Although the exact strategy for the future analysis is yet to be determined, some potential work could include: precise measurement of the differential cross-sections associated with $H \rightarrow \gamma\gamma$ decays, a study of the cross-sections of Higgs production mechanisms resulting in decays to two photons, and a focus on the $H \rightarrow \gamma\gamma$ decay with associated b quark production... (FIXME check)

In run II, the LHC will ramp up the centre of mass energy of collisions \sqrt{s} to 13TeV and eventually to 14TeV. This increase, coupled with a rise in the luminosity of the beam (FIXME check!) should usher in the era of precision Higgs physics. The tradeoff to pay, however, is that further strain will be put on the trigger, reconstruction and event processing frameworks, both during data acquisition and after. For example, the number of additional (uninteresting) interactions within a bunch crossing, known as pileup, will increase, thus causing problems for triggering, track reconstruction and energy resolution. In order to make the most of the opportunities offered by run II, much work needs to be done to ensure that the CMS collaboration is ready to deal with these challenges when the LHC switches back on in March 2015, less than a year from now.

One example of where such work is required is in the calibration of the electromagnetic calorimeter (ECAL) subdetector. Because the $H \rightarrow \gamma\gamma$ analysis deals with photons, intrinsically electromagnetic objects, its sensitivity relies heavily on the performance of the ECAL. In run I, the excellent sensitivity of the subdetector allowed the analysis to play a leading role in the discovery of the Higgs boson and the subsequent analysis of its properties. Naturally, in order to make further and more precise measurements in run II, the ECAL’s performance must be improved, or at least maintained, despite the challenges of the $\sqrt{s} = 13\text{TeV}$ environment.

To cope with these changes, the CMS collaboration has taken various steps. One of the key changes affecting the ECAL is an update of the CMS software, which reconstructs particles from the raw data. A holistic “particle flow” method is being implemented, allowing information from various subdetectors to be used in a holistic way. Specifically, this affects the reconstruction of electrons and photons within the tracker and ECAL: in short, the way in which energy deposits are clustered within the array of ECAL crystals is being modified to allow more complicated shapes. This new reconstruction method has the advantage of being able to mitigate the effects of pileup, but represents a fundamental shift in the treatment of electromagnetic objects. Although in principle this innovation should lead to energy resolutions at least as good as those enjoyed by the ECAL in run I, it needs to be thoroughly tested and validated to ensure good performance in run II. Helping to validate this new clustering method is an aspect of the service work which I have pledged to complete in order to become an author in CMS collaboration papers.

Another important task, this time within the $H \rightarrow \gamma\gamma$ group specifically, is to publish a final analysis of the sensitivity achieved by the group’s efforts during run I. In this way, it will be possible to learn from the experience of run I, and benchmark any potential improvements in the group-specific software and analysis tools (indeed, the software is being redesigned in order to cope with the group’s changing membership and physics objectives). I was involved in one aspect of this work, namely the measurement of the individual photon energy resolutions afforded by the $H \rightarrow \gamma\gamma$ software, `h2gglobe`. The plots I produced are to be included in an upcoming paper on the topic of photon reconstruction in run I (CITE arxiv at least FIXME).

This document is designed to communicate the research I have undertaken during the first nine months of my Ph.D. As such, I will present an overview of the work and findings from my efforts within the $H \rightarrow \gamma\gamma$ group and the ECAL detector performance group (DPG). I will also provide context to these results by giving a brief summary of developments in particle physics leading up to the modern day, an outline of Higgs physics at the LHC, and overview of the CMS detector.

2 The SM and $H \rightarrow \gamma\gamma$

2.1 The Standard Model

The standard model (SM) of particle physics came into being in the mid-1970's, when the discovery of the J/ψ particle [1, 2] and results from deep inelastic scattering experiments at SLAC confirmed the predictions of quark models. The SM has been an immensely successful theory, accurately describing many processes in high energy physics. Among other features, the model placed all fundamental forces apart from gravity into one framework, and united the electromagnetic and weak forces into the electroweak force [3–5]. In order to do this, a mechanism was required to permit the W^\pm and Z vector bosons to have mass while allowing the photon to remain massless. Crucially, this process was required to preserve gauge invariance. Such a theory was independently proposed by several theorists [6–11], and is commonly referred to as the Higgs mechanism. In 1964, Higgs postulated that one outcome of this mechanism was that it should yield an observable particle, the Higgs boson [8]. Over the decades, the particles postulated by the SM were discovered: the τ lepton in 1975 [12], the b quark in 1977 [13], the gluon in 1979 [14–16], the Z and W^\pm bosons in 1983 [17, 18], the top quark in 1995 [19, 20] and the ν_τ in 2000 [21]. Each new discovery cemented the SM as one of the most successful theories of modern times. By the turn of the millennium, all but one particle postulated by the SM had been observed: the Higgs boson, which had proved elusive despite decades of searches. The Higgs search prompted the construction of the Large Hadron Collider (LHC) at CERN, and two multi-purpose detectors, ATLAS and CMS, were designed with the Higgs observation as one of their main physics goals. In 2012, the two experiments jointly announced the observation of a Higgs-like particle of mass ~ 125 GeV, ending a 50-year lull between postulation and discovery [22, 23].

Although the SM has been very successful as a theory, it falls short of being a “theory of everything”, and is clearly incomplete. For instance, it does not accommodate mass terms for neutrinos, which are required to explain the origin of neutrino oscillations observed in many experiments [24–26]. Furthermore, it does not contain a viable candidate for dark matter, which is needed to explain the mass deficit of the universe [27]. Other issues such as the hierarchy problem [28] and the origin of matter-antimatter asymmetry in our universe [29] also persist. Clearly, the SM is incomplete or approximate, and many efforts in modern high energy physics are being made to discover “Beyond the Standard Model” (BSM) physics. Supersymmetry proposes one such extension to the SM, but many other models exist, and the search for new physics will be one of the primary objectives of experimentalists during run II of the LHC in 2015.

Even in the Higgs sector, more work remains to be done. Precision measurements of the properties of this particle are needed: does it behave like the SM predicts? Is there only one such particle? Detailed studies are required to ascertain couplings, the differential cross section, width and other attributes of this Higgs particle. Deviations from the expected values of such properties could provide valuable insight into the nature or indeed existence of BSM physics.

2.2 $H \rightarrow \gamma\gamma$

According to SM, the Higgs boson’s coupling with particles is proportional to their mass. As such, its production modes in the environment of the LHC are dominated by interactions involving the heavier particles of the SM. Typically, the Higgs boson is produced by one of the following mechanisms (Fig. 1):

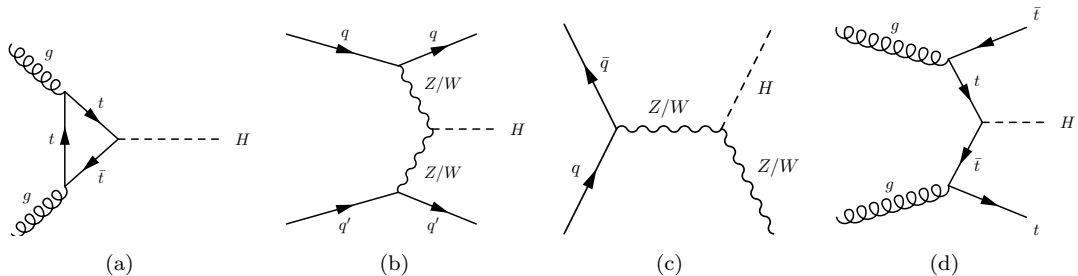


Figure 1: Higgs production modes at the LHC: (a) gluon-gluon fusion, via a loop of top quarks, (b) vector boson fusion (VBF), with associated quark production, (c) associated vector boson production (also known as “Higgsstrahlung”) and (d) top quark fusion with associated top quark production.

By the same token, the SM Higgs boson decays to pairs of particles with branching ratios proportional to the square of their mass. The production of a pair of t quarks is not kinematically allowed because their mass is high, so the most likely decay modes are $H \rightarrow ZZ$, $W^\pm W^\mp$, $b\bar{b}$ and $\tau^+\tau^-$. In addition, a small fraction of decays of the Higgs boson (< 1%) can occur via a loop diagram to a pair of high-energy photons. The branching fractions and cross sections of these production and decay modes are available in the Handbook of LHC Higgs Cross Sections [30,31].

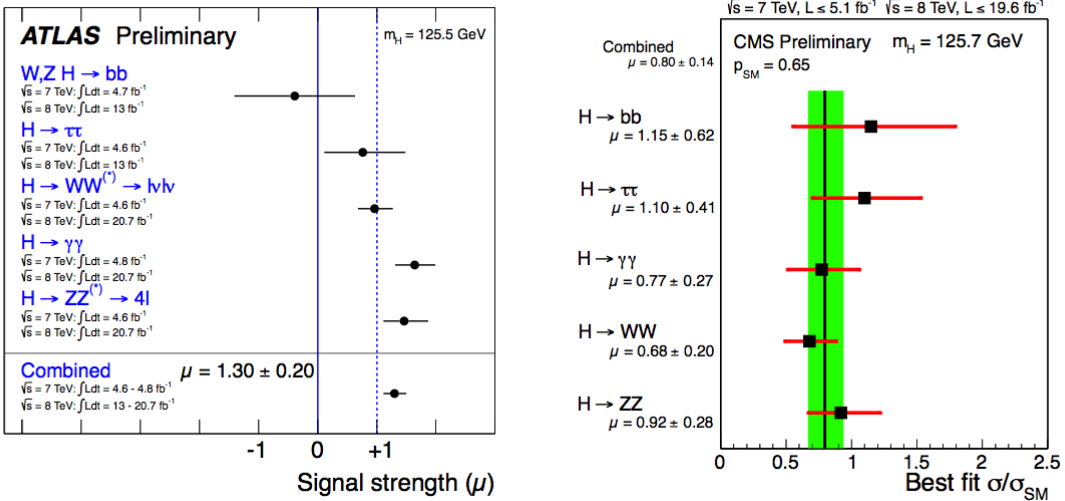


Figure 2: Signal strengths of the Higgs boson observations by decay mode and in combination at ATLAS (left) and CMS (right), consistent with the observation of a particle of $m_H \sim 125$ GeV [32].

The Higgs boson was discovered in 2012 using data from runs at $\sqrt{s} = 7$ and 8 TeV, and was found to have a mass $m_H \sim 125$ GeV. The signal strengths of the various decay modes at the CMS and ATLAS experiments can be seen in Fig. 2. Despite fewer than 1% of Higgs boson decays occurring via $H \rightarrow \gamma\gamma$, this channel played a crucial role in the discovery, and remains one of the two most sensitive methods of studying the Higgs boson. This is in part thanks to the excellent performance of the CMS ECAL.

3 The CMS detector

3.1 Overview of the LHC and CMS

The LHC is a synchrotron that was built in the tunnel which previously contained the Large Electron Positron (LEP) collider at CERN, near Geneva. It has a circumference of 27km and was designed to collide beams of protons (or lead ions) head on. In its latest run, it achieved a centre of mass energy of $\sqrt{s} = 8$ TeV. The LHC shut down for a planned upgrade period in 2012, and is due to restart collisions in March 2015. At this stage, it should be able to deliver a centre of mass energy close to $\sqrt{s} = 13$ TeV, before ramping up to its design value of 14 TeV. As mentioned previously, the LHC is equipped with two multi-purpose detectors, CMS and ATLAS, which simultaneously discovered the Higgs boson using the data from run I. This report will focus on the CMS detector, the overall layout of which can be seen in Fig. 3 below [33].

CMS, which stands for Compact Muon Solenoid, is located approximately 100m underground at point 5 of the LHC, near the french village of Cessy. It is a layered detector over 21m long and 14m in diameter, weighing over 12,500 tons. It consists of a superconducting solenoid magnet 13m long and 5.9m in diameter, generating a 3.8T magnetic field, which is embedded within the various subdetectors. The high magnetic field allows for good energy resolution in the compact space of the detector. CMS is composed of a cylindrical barrel region around the solenoid, and two endcaps on either side. Four layers of iron act as a return yoke for the magnet and house muon detector chambers (drift tubes in the barrel region and cathode strip chambers in the end cap region). The calorimeters (electromagnetic and hadronic) and inner tracker are housed within the solenoid.

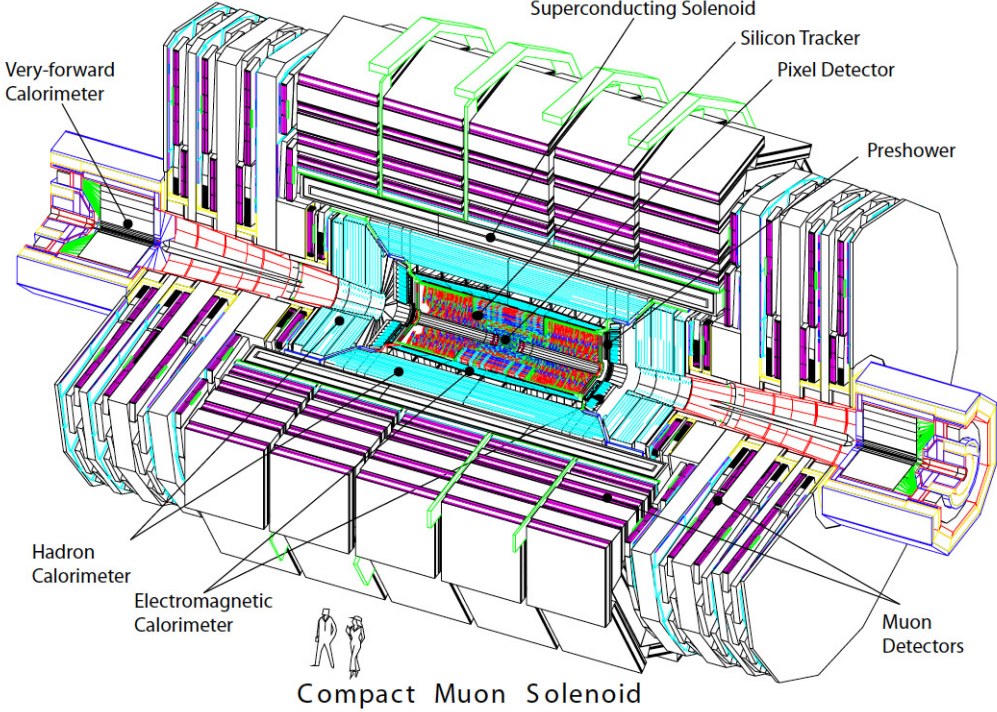


Figure 3: The CMS detector perspective view.

The CMS detector uses a right-handed coordinate system whereby the x -axis points towards the centre of the LHC ring, the y -axis points upwards, and the z -axis points in the direction of the counter-clockwise beam. A coordinate system more convenient to the geometry of the detector is (η, ϕ, z) , where $\eta = -\ln[\tan(\frac{\theta}{2})]$ is the pseudorapidity (where θ is the polar angle relative to the beam axis) and ϕ is the angle relative to the y -axis in the (x, y) plane.

3.2 The electromagnetic calorimeter (ECAL)

The ECAL is the subdetector which the $H \rightarrow \gamma\gamma$ uses most (and indeed, almost exclusively), and is also the subject of my servicework. This report will therefore deal with it in a more detailed manner than it will for the other subdetectors. This information from this section is taken from [33] and [34].

The ECAL is made up of an array of 61,200 lead PbWO₄ (lead tungstate) crystals in the barrel section and 14,648 crystals in the end caps, arranged one crystal deep. PbWO₄ was chosen because it has a short radiation length (the mean distance over which an electron loses all but $\frac{1}{e}$ of its energy to bremmstrahlung) of 0.89cm, a small Molière radius (the radius of a cylinder containing on average 90% of a shower's energy) of 2.19cm and because it is a fast scintillator. This is a central feature of the CMS detector as it allows for excellent energy resolution of incoming photons.

The crystal front faces are 22mm \times 22mm squares, corresponding to approximately $\delta\eta \times \delta\phi = 0.0174 \times 0.0174$, roughly matching the Molière radius. The individual crystals thickness is approximately 26 radiation lengths, to ensure that the electromagnetic showers are fully contained within the ECAL. The array of crystals extends to $|\eta| = 3$, but precision measurements are only made up to $|\eta| = 2.5$. There are also transition regions between the ECAL barrel and endcaps around $|\eta| = 1.5$ where data is not taken. The arrangement of the crystals in the ECAL can be seen on Fig. 4.

The crystals are attached to photodiodes, which read out the amount of light, and thus the amount of energy, deposited within by the showers. The resolution of the ECAL is modelled with the equation

$$\left(\frac{\sigma}{E}\right)^2 = \left(\frac{S}{\sqrt{E}}\right)^2 + \left(\frac{N}{E}\right)^2 + C^2 \quad (1)$$

where S represents the stochastic term, N represents the noise terms and C represents a constant term [35]. The design values of these parameters are approximately $S = 2.8\%$ GeV $^{\frac{1}{2}}$, $N = 0.12$ GeV and

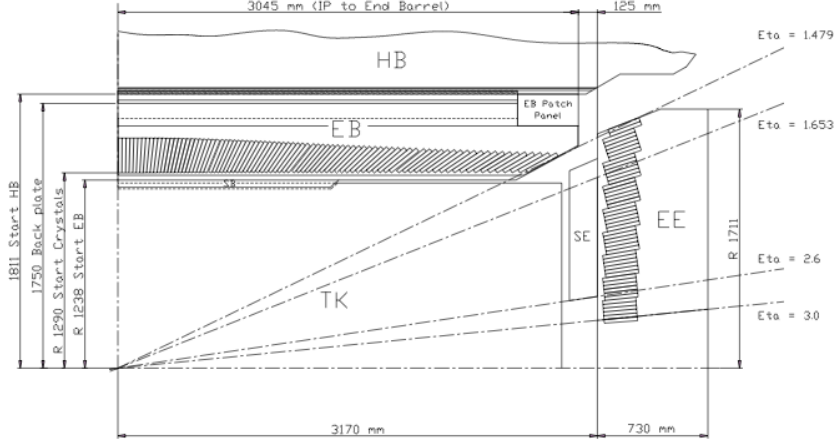


Figure 4: Schematic cross section of one quadrant of the ECAL, showing the arrangement of crystals in the ECAL Barrel (EB) and Encaps (EE) [34]. The shower detector (SE) is also visible, as is the hadron calorimeter barrel (HB) and the tracker (TK).

$C = 0.3\%$. The performance of the ECAL matched these design values during the 2012 run [36].

The ECAL is split into the barrel (EB) and the endcaps (EE), which have notably different structures and performance. The EB provides coverage in the region $|\eta| < 1.479$, while the EE provides coverage for $1.556 < |\eta| < 2.5$. The crystals in the EB are grouped into 36 supermodules, each subtending an angle of 20° in ϕ . The crystals are arranged so that they do not point directly at the mean position of the primary interaction vertex, but instead are positioned with a 3° offset in both θ and ϕ . This is done to help avoid particles being lost in the gaps between the crystals. The EE is composed of two “D”-shaped sections, built up of “supercrystals” (units of 36 standard crystals). The position of the endcaps causes them to endure higher levels of radiation than the barrel region do, and therefore the EE must be made with more radiation-hard materials. This factor, along with a high flux of particles and worse clustering algorithms, means that the EE has notably worse resolution than the EB.

The ECAL is also mounted with preshower detectors (SE) at $1.54 < |\eta| < 2.61$, the main purpose of which is to distinguish between π^0 and γ particles. The SE is composed of two planes of Pb, of 2 and 1 radiation lengths respectively, with high granularity silicon detector strips after each. The SE is used in cases when pions from jets undergo $\pi^0 \rightarrow \gamma\gamma$, where both photons strike the same crystal. Although the EE might interpret this as one highly energetic photon, the high granularity of the silicon strips in the SE allow two tracks to be identified. The energy deposited in the SE is measured, and an appropriate correction is made to the energy measured in the ECAL crystals.

3.3 Other subdetectors

The closest subdetector to the beam crossing point is the inner tracker [37], which is used to accurately measure the momenta of charged particles, and thus reconstruct the positions of primary and secondary interaction vertices. The inner tracker consists of a barrel section (3 cylindrical layers of silicon pixel detectors close to the interaction region, surrounded by 10 layers of silicon micro-strip detectors), and endcaps (two discs of silicon pixel detectors and 12 discs of silicon micro-strip detectors). Momenta of charged particles can be measured accurately for $|\eta| \leq 1.6$ (where particles intersect about 13 planes), and to a lesser extent for $|\eta| < 2.5$ (where particles intersect at least 8 planes), by measuring the curvature of tracks as they bend in the strong magnetic field. The tracker is encased within the ECAL.

The hadronic calorimeter (HCAL) surrounds the ECAL. This subdetector is used to measure the directions and energies of quarks, gluons in the form of jets and estimate the directions and energies of neutrinos by looking at the amount of missing transverse energy. The CMS HCAL is a sampling calorimeter, consisting of active material between absorber plates. The active material is a plastic scintillator read out by wavelength-shifting plastic fibers. The absorber plates are made of a copper alloy (copper is chosen as it is a non-magnetic material, and thus will not be affected by the strong magnetic field within the solenoid). The HCAL provides coverage up to $|\eta| < 3$. In order to accurately measure

missing energy, the HCAL must be as hermetic as possible. For this reason, an additional “forward” calorimeter is appended, which gives coverage up to $|\eta| < 5$. This uses active quartz fibers within a copper absorber matrix. [38]. The HCAL is ancased within the solenoid.

Finally, the solenoid is surrounded by the outermost subdetector, the muon system, which also functions as a return yoke. Again, this subdetector is segmented into a cylindrical barrel region and two endcaps. The in barrel, the muon tracking is provided by four layers of drift tubes, interspersed with the iron return sections. This section of the muon system has coverage to $|\eta| < 1.3$. In the endcaps, the muon tracking is composed of four layers of cathode strip chambers. [39]

4 The $H \rightarrow \gamma\gamma$ analysis

4.1 Overview of the legacy analysis

The $H \rightarrow \gamma\gamma$ analysis relies on the fact that there is a small but non-negligible branching fraction of Higgs bosons which decay to two highly energetic photons via loops of particles, generally virtual top quarks or W^\pm vector bosons. Although around the mass $m_H \sim 125$ GeV there is a large irreducible QCD background, the excellent diphoton energy resolution ($\sim 1\%$) of the CMS ECAL allows the reconstruction of a narrow peak above the background. The resolution available via this decay channel meant that it was identified early on as “one of the most promising channels in the search for a SM Higgs boson in the low mass range” [40]. The following description is based on the “mass-factorised multivariate analysis” (referred to within the group as the MVA) of the $\sqrt{s} = 7$ and 8 TeV data samples [41].

The analysis depends heavily on boosted decision trees (BDTs) to identify and classify events. A BDT is an algorithm which categorises items based on multiple input variables [42]. Different weights are applied depending on whether an item passes or fails cuts based on these input variables. The weights are summed at the end and the final value is used to determine which category the item falls in. The algorithm is trained (i.e. the aforementioned weights and cut thresholds are determined) with simulations or data with similar properties.

The first step in the analysis is to identify candidate diphoton events. There is a loose trigger, identifying any pair of photons in an event based on ECAL isolation, shower shape and energy. A more stringent selection takes place later to choose only diphoton events likely to have originated from a Higgs decay.

The next step is to locate the photon production vertex. This is an important step because an accurate determination of the origin of the photon tracks can be combined with the measured ECAL energies and spatial location of the photon showers to accurately reconstruct the Higgs 4-momentum, and thus its invariant mass. A simple analysis of conservation of 4-momentum in the laboratory frame yields the required formula:

$$m_H = m_{\gamma\gamma} = \sqrt{2E_1 E_2 (1 - \cos \alpha)} \quad (2)$$

where $m_{\gamma\gamma}$ is the invariant mass of the diphoton system, $E_{1,2}$ are the energies of the reconstructed photons and α is the opening angle between the two photons. It is clear that since the ECAL resolution is excellent, $E_{1,2}$ are well known. The only other contribution to the mass resolution comes from the opening angle α . In order to accurately measure this angle, the photon creation vertex must be identified to within 10 mm of its true position. If this is the case, the error contribution from α is negligible.

Vertex identification can be achieved by matching the kinematic properties of the tracks coming from these vertices with the diphoton system’s transverse momentum. Another option is to use information from the tracker if the photon converted into an e^+e^- pair: in this case the track directions can be combined with the impact position in the ECAL to extrapolate back to the photon production vertex. A BDT trained on simulated data is used to identify the vertex, using quantities such as those mentioned above as input variables. The vertex identification efficiency is measured to be of the order of 80%, and the associated systematic uncertainty is well understood.

Since the photon pairs expected from Higgs decay should be highly energetic, offline cuts are applied to select candidate diphoton events likely to have originated from a Higgs boson decay. These cuts are defined as $E_T > m_{\gamma\gamma}/3$ for one candidate photon and $E_T > m_{\gamma\gamma}/4$ for the other [43], where E_T is the transverse energy of the photon and $m_{\gamma\gamma}$ is the invariant mass of the diphoton system. It is possible that a photon may have pair converted ($\gamma \rightarrow e^+e^-$) before reaching the ECAL. Such occurrences are identified using the variable R_9 , defined as the sum of the energy of the 3×3 array of lead tungstate crystals centred around the most energetic crystal in the supercluster, divided by the total energy of said

supercluster. A value of R_9 smaller than 0.94 is indicative of a photon having undergone pair conversion. R_9 is used as an input variable in a BDT which classifies events based on their sensitivity, as described below. A further BDT is also used to remove “non-prompt” photons (i.e. photons not created at the primary vertex) and other particles misidentified as photons, such as pions.

The events are then segmented into categories based on the expected signal to background ratio and diphoton invariant mass resolution. Studying these separately increases the overall sensitivity of the analysis. An additional categorisation where candidate events also pass a dijet trigger corresponds to VBF Higgs production (See figure 2.b: the quarks are scattered at a sufficiently large opening angle for them to undergo hadronisation and form jets rather than be lost down the beam-pipe). This mode is analysed separately because its signal to background ratio is over an order of magnitude better than for the other categories [43]. The categorisation is achieved using another BDT, where the input variables are chosen to be dimensionless to avoid any bias in the mass distribution. For example, the transverse momenta of the photons are used amongst other input variables, but they are scaled by the calculated diphoton invariant mass to yield a dimensionless criterion.

The background model is obtained using a data-driven technique rather than a MC prediction, as this avoids any systematic uncertainties based on mis-modelling. For each of the categories, the diphoton mass distribution outside of the region of interest is fitted. The function used to fit the data is chosen based on minimisation of the bias introduced in each case. Candidate functions involve exponentials, power laws, polynomials and Laurent series. The bias is found to be negligible when Bernsteins of order 3 to 5 (depending on the category) are used.

Finally, the observed invariant mass distribution is compared to that predicted by the background fit. An observed excess of events around ~ 125.0 GeV with a local significance of 4.1σ in the $\gamma\gamma$ decay channel signalled the existence of the Higgs boson in 2012. Combined with measurements from other decay modes, CMS announced a measurement of $m_H = 125.3 \pm 0.4(\text{stat.}) \pm 0.5(\text{syst.})$ GeV with a local observed significance of 5.0σ [41].

Another, slightly less sensitive method, known as the “cuts in categories” or CiC method, was used as a cross-check to the MVA method. The CiC method differs from the MVA in the number of categories: the former segments events broadly into just four categories in R_9 and $|\eta|$.

4.2 Photon resolution studies

4.2.1 Motivation

An important task after the publication of the legacy analysis is to learn lessons from the performance during run I, so that any future improvements can be benchmarked. As such, a paper is being prepared to mark the performance of the $H \rightarrow \gamma\gamma$ analysis during the later part of the first run. One aspect of this was to run a study to look at the resolution of photon energies as reconstructed using the $H \rightarrow \gamma\gamma$ software package, known as `h2gglobe`. I was tasked with preparing this plot.

The study consisted of looking at the reconstruction of Higgs boson decay photons in simulated collision at 8TeV, assuming $m_H = 125\text{GeV}$. The resulting plot was intended to give the effective energy resolution σ_{eff}/E for individual photons in the ECAL, segmented into small $|\eta|$ bins. Monte Carlo samples for the 8TeV LHC conditions were used in this study. More precisely, a sample of simulated $H \rightarrow \gamma\gamma$ events corresponding to each Higgs production mode (VBF, gluon-gluon fusion, associated Z/W^\pm production and associated top quark production), weighted by cross section, were used as the dataset for the study. Since the intention was to provide an account of the sensitivity of the $H \rightarrow \gamma\gamma$ analysis, the MC samples were passed through the globe MVA framework, and therefore were processed as they would have been in the legacy analysis, with full smearing and corrections.

4.2.2 Method and Result

In order to produce the required plots, the `h2gglobe` MVA framework code was modified so as to produce an additional ROOT `TTree` (FIXME citation), containing only the information needed for this study. The writing of this additional `TTree` took place after all the actual analysis within the framework was complete, so the results incorporate all the required corrections.

In order to measure the effective energy resolution, it was necessary to compare the *true* energy of the photons E_{true} (as generated in the simulation) with the *reconstructed* energy of the photons E_{reco} (as provided after reconstruction and application of corrections in the `h2gglobe` framework). To make this comparison in a meaningful way, the generated and reconstructed photons needed to be

matched correctly. This was done using an unambiguous geometrical method: for each generated photon in an event, the value of $\Delta R = \sqrt{\Delta\eta^2 + \Delta\phi^2}$ (where Δ refers to the difference between generated and reconstructed values of the quantity) was calculated for the two reconstructed photons. The reconstructed photon minimising the value of ΔR was chosen as the match for that generated photon.

For each event, both photons were individually categorised first by $R_9 < 0.94$ or $R_9 \geq 0.94$, then by their $|\eta|$ position within the detector. The width of the $|\eta|$ categories was 0.1, apart from the region near the transition between the ECAL barrel and ECAL encap, where the data are excluded (resulting in two slightly larger categories on either side, namely $1.3 \leq |\eta| < 1.4442$ and $1.566 \leq |\eta| < 1.7$), thus 23 categories. Taking into account the two R_9 options, this left 46 photon categories. For each one, a histogram of the values of E_{reco}/E_{true} was created. An algorithm was used to calculate σ_{eff} (defined as half the width of the smallest window containing 68.3% of events in a distribution). This algorithm recursively scanned potential windows in the histogram until the smallest one matching the required condition was found. A different algorithm also calculated the “Full Width Half Maximum” (FWHM), which is the width of the peak when measured at half of its maximum height. In this case, the algorithm fitted each histogram to a combination of a Gaussian and a Crystal Ball (FIXME citation) function, then created a very finely binned histogram of the best fit. The bin with the largest number of events was identified, and then the distance between the first bin with half that number of events, and the last bin with half the number of events was returned. For a true Gaussian distribution, $\sigma_{eff} = \sigma = FWHM/2\sqrt{2\ln 2} \simeq FWHM/2.35$. In other cases, $\sigma_{eff} \geq FWHM/2.35$. Fig. 5 shows examples of these histograms.

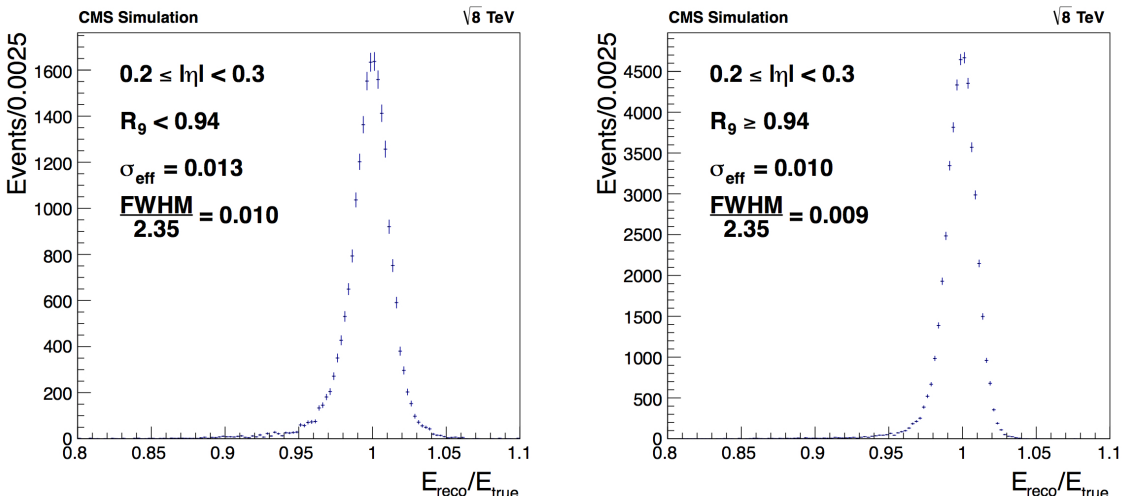


Figure 5: Example E_{reco}/E_{true} histograms for two $|\eta|$ and R_9 categories. The vertical axis indicates the number of events per bin if each event were counted with the weight of a gluon-gluon fusion event. Overlaid on each plot is the calculated value of σ_{eff} and $FWHM/2.35$. For a distribution with a Gaussian peak but non-Gaussian tails, we expect $\sigma_{eff} \geq FWHM/2.35$, which is what is observed.

The values of FWHM were not used in the rest of the study, however they provided a good sense check that the distributions made sense. On the other hand, σ_{eff} was used as the input for the main result. The values of σ_{eff} for the distributions of E_{reco}/E_{true} are equal to σ_{eff}/E (FIXME why??), and were used as inputs to the effective energy resolution plot. Each of the 46 $|\eta|$ and R_9 categories provided a value, which was then plotted versus $|\eta|$ to give the main plot (Fig. 6).

As expected, the effective resolution is consistently worse for low R_9 categories than for their high R_9 equivalent. This is because low R_9 photons are more likely to have undergone pair conversion, and the resulting electrons and positrons may have emitted energy via bremmstrahlung before hitting the ECAL. Furthermore, the categories where $|\eta|$ lies over a supermodule boundary (vertical dashed lines) have worse resolution than neighbouring categories. This is also expected, as the interfaces between the supermodules are less hermetic than the faces of the supermodules, leading to energy lost between the gaps. Finally, the resolution in the endcaps (ie categories where $1.5 \leq |\eta| < 2.5$) is substantially worse than the resolution in the barrel, as expected.

To sum up, this study set out to estimate the individual photon resolution in small $|\eta|$ bins in the

CMS ECAL for simulated $H \rightarrow \gamma\gamma$ events at $m_H = 125\text{GeV}$, after the full and final corrections of the h2gglobe MVA framework had been applied. The result is that for high R_9 photons, the effective energy resolution is of the order of $\sim 1\%$ in the barrel and $\sim 2.5\%$ in the encaps. For low R_9 photons, the resolution is slightly worse.

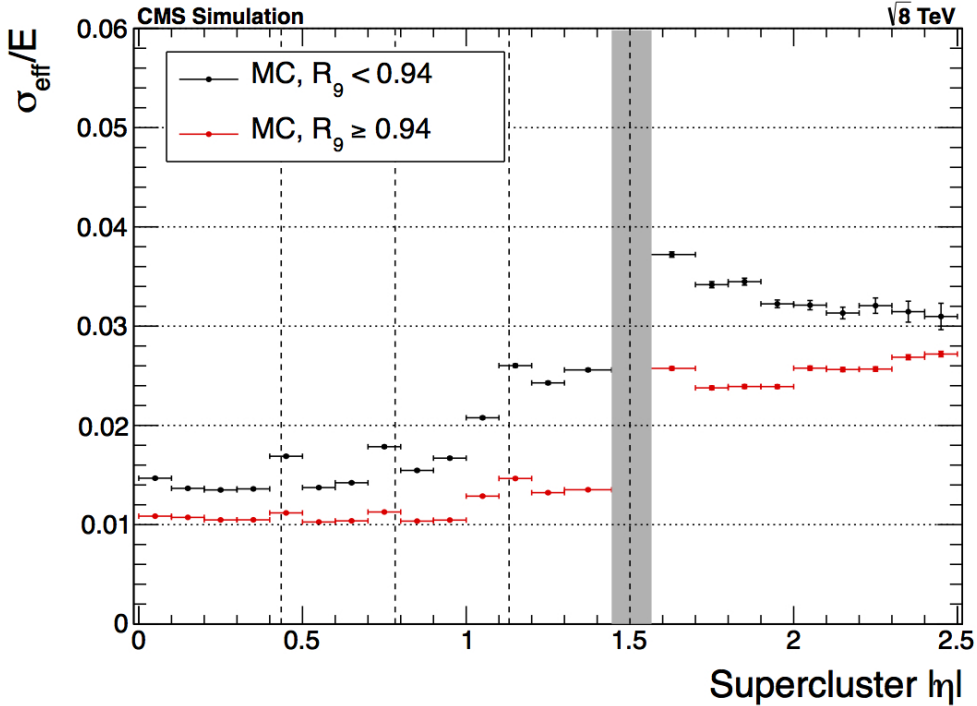


Figure 6: σ_{eff}/E plotted in 23 $|\eta|$ bins and two R_9 categories. The horizontal dotted lines are shown as guides only. The Vertical dashed lines show boundaries between supermodules. The grey band indicates the interface between the ECAL barrel and encap regions, which is not studied. The horizontal error bars indicate the width of the $|\eta|$ bin, while the vertical error bars (visible chiefly in the high $|\eta|$, low R_9 categories), indicate the estimated uncertainty on the measurement of the resolution.

4.2.3 Estimation of the error

The vertical error bars in Fig. 6 provide an estimate of the uncertainty associated with the measurement of the resolution in each $|\eta|$ and R_9 category. The error for a given category was assumed to be at least as large as the standard statistical error, given by $\text{Err}_{\text{stat}} = \sigma_{\text{eff}}/\sqrt{2N}$ (where N is the number of photons in the category). However, additional systematic uncertainty may have been added by the algorithm used to calculate σ_{eff} . To check this, the sample was divided into ten equivalent subsamples. For each subsample, the entire study was rerun, and the resulting ten values of σ_{eff}/E were recorded for each of the 46 $|\eta|$ and R_9 categories. The RMS error of these ten values was calculated in each case. If the actual error really were equal to Err_{stat} , we would expect that the subsample RMS error in each category would be $\sim \sqrt{10} \simeq 3.2$ times larger than the error for the full sample. However, when comparing the calculated subsample RMS error to the minimum statistical error for each category, the factor was on average 4.4 rather than 3.2, indicating that the true error is (very roughly) 1.5 times larger than Err_{stat} . As a result, the error added into Fig. 6 was $\text{Err}_{\text{stat}} \times 1.5$, thus providing a rough estimate of the uncertainty of the resolution. For most bins, the fact that N is very large means that the vertical error bars are completely invisible, however for low R_9 , high $|\eta|$ categories, which have fewer photons, the error bars are no longer negligible.

4.2.4 Checks

Several checks were performed during the course of the study in order to verify the consistency of the results. The main ones are summarised here. Firstly, the photon matching mechanism was checked thoroughly. The good performance of the mechanism can be seen in Fig. 7.

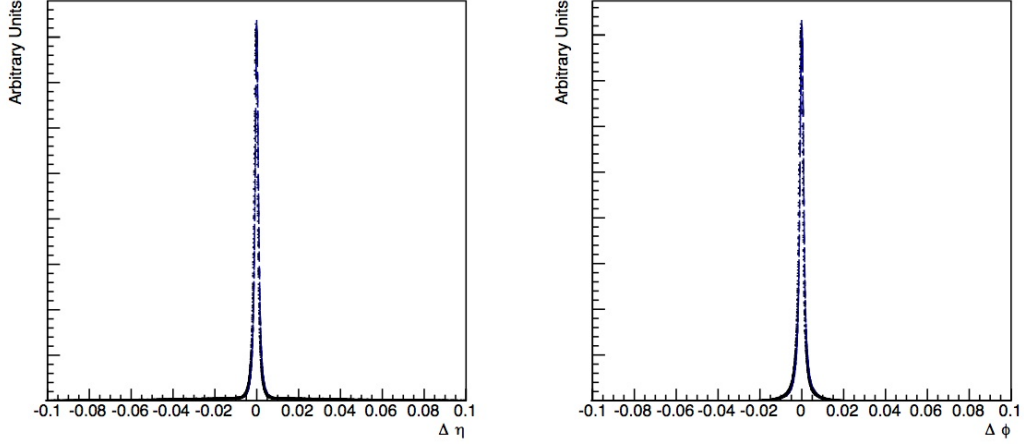


Figure 7: The plot on the left (right) shows $\Delta\eta$ ($\Delta\phi$) for photons used in this study, where ΔX refers to the difference between X_{reco} and X_{true} . The resulting distributions are very narrowly centered about 0, showing that the matching algorithm is performing very well. In the rare cases where $\Delta\eta$ and $\Delta\phi$ are different from 0, this is due to poor reconstruction of photons rather than mismatching.

Secondly, the study was also run using the CiC `h2gglobe` framework. Since the CiC framework was used as a crosscheck for the MVA framework in the actual legacy analysis, it provided an excellent opportunity to check consistency in this study. As can be seen in Fig. 8, the CiC version leads to slightly worse resolution in the endcaps for low R_9 , which is as expected since the MVA framework was designed to be more sensitive in this region.

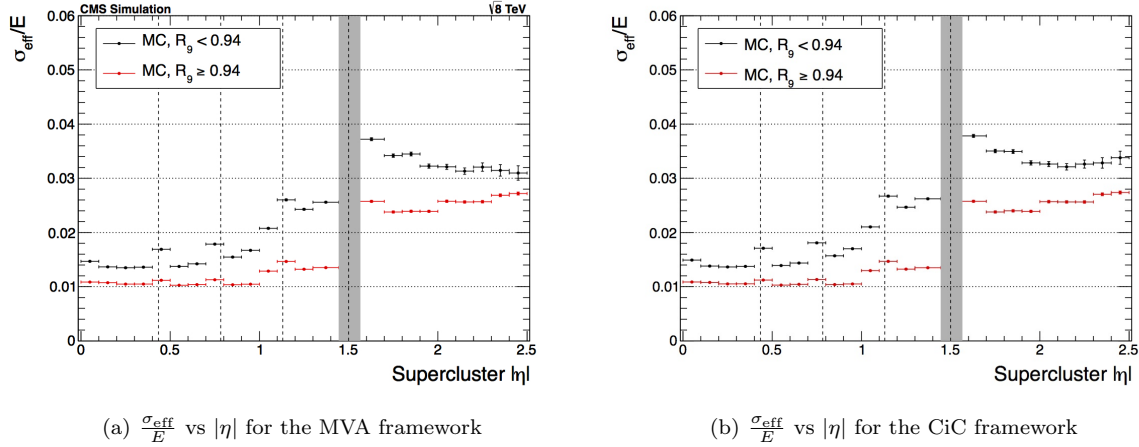


Figure 8: (a) shows the final result when the initial data are run through the `h2gglobe` MVA framework, while (b) shows the same plot when the CiC framework is used. The results are almost identical, with the biggest differences observable in the low R_9 , high $|\eta|$ categories. This is as expected, as the MVA analysis was designed to be more sensitive, especially in this region.

A final check was run to check whether modifying the binning in of the $E_{\text{reco}}/E_{\text{true}}$ plots had an effect on the result of the σ_{eff} algorithm. Various bin sizes were considered, however, the change in the resulting values of σ_{eff} were negligible.

5 ECAL clustering validation service work

5.1 Overview of the task

The CMS Software is called **CMSSW**, and is defined as follows. “*The overall collection of software, referred to as CMSSW, is built around Framework, an Event Data Model, and Services needed by the simulation, calibration and alignment, and reconstruction modules that process event data so that physicists can perform analysis.*” [44]

Effectively, **CMSSW** provides a way to process and select events from raw data and allows physicists in the CMS collaboration to run analyses and produce physics results. One way in which **CMSSW** does this is in the reconstruction of particles. Of particular interest to the $H \rightarrow \gamma\gamma$ group is the way in which particles are reconstructed within the ECAL. The latest version of **CMSSW** is known as **CMSSW_7_0_X** (we shall refer to it as **70X** for short), where the **X** can represent a number of different sub-versions. A key distinction between this and the version used during run I, **CMSSW_5_3_X** (referred to as **53X** for short), is indeed the way in which photons and electrons are reconstructed.

The ECAL measures energy of impacting particles by estimating the amount of energy deposited by electromagnetic showers within its crystals. However, since the crystals are roughly the size of Molière radius of PbWO_4 (which contains 90% of the shower), it is clear that some of the energy from a single shower will be spread over a number of neighbouring crystals. Therefore, to get the best measurement of energy, neighbouring crystals are “clustered” together [45]. There are two main strategies for clustering: The cluster is either a fixed matrix around the local maximum (useful when showers have much higher energy than the “noise” in the detector) or a dynamic shape, where energy deposits around the maximum are summed until a noise floor threshold or a different cluster is found.

On the one hand, **53X**, broadly speaking, uses a fixed matrix approach, where the cluster is 5x5 crystals η and ϕ . However, tracks of electrons from events or pair converting photons will bend in ϕ under the influence of the 3.8T magnetic field. As they bend, they may radiate photons through bremmstrahlung. So, a particle may produce energy deposits which spread out in the ϕ direction. In order to properly reconstruct the energy of such electrons of pair-converted photons, **53X** uses a dynamic extension in ϕ to pick up sub-clusters.

70X, on the other hand, has implemented a holistic “particle flow” (PF) [46] approach to reconstructing events throughout the the whole detector. To do this, even small deposits from other objects needs to be reconstructed, so that they can be used to construct overarching PF jets and calculate missing transverse energy. As part of this, a dynamic shape clustering method has been implemented, which uses information from neighbouring crystals to identify the shape of a cluster, then a performs a regression to estimate the energy of the shower. In this method, all ECAL objects (electrons and photons) are reconstructed with the same algorithm and undergo particle identification at a different time. This method was implemented because it is able to take advantage of the ECAL granularity to improve containment of electrons and photons while rejecting pileup (a key challenge in the environment of run II) by using a noise floor threshold.

However, although in principle the new clustering method should provide some benefits, especially for low transverse momentum objects, it needs to be validated. Any significant loss in the energy resolution of ECAL objects could have a potentially disastrous effect on the $H \rightarrow \gamma\gamma$ analysis in particular, but in general on CMS’s capability to make important measurements in run II. My service work therefore is to work with the ECAL detector performance group (DPG) to help check the performance of new clustering method in **70X** versus **53X**.

5.2 The ECALELF tool

The **ECAL Calibration with Electron Framework (ECALELF)** is a generic tool which uses $Z \rightarrow e^+e^-$ events to monitor and calibrate the ECAL (CITE twiki FIXME). **ECALELF** works within **CMSSW** to provide aligned and calibrated data upon which tests and studies can be run. In this sense, it is an ideal tool to validate the new clustering method for electrons, and can be adapted to validate the clustering of photons also. The general workflow for calibration with **ECALELF** is to take **RECO** data and **MC** (ie, raw data which has been reconstructed using the native **CMSSW** version), and apply a selection to retrieve only candidate $Z \rightarrow e^+e^-$ events. A further selection is made via BDT to reduce to pool of candidate events. Once this is complete, a map is made between **MC** and data events based on finely segmented η and R_9 categories for each electron (note that the definition of R_9 for electrons is the same as that for

photons. $R_9 < 0.94$ is indicative of an electron which has lost a lot of energy through bremmstrahlung, while $R_9 \geq 0.94$ indicates it has lost only a small fraction of energy). The calibration can then be made, as described below.

The objective of the calibration is to provide an energy-dependent correction to apply to individual electrons in each category, in order to make the invariant mass distribution from the data match the distribution from the MC. However, in general, the two electrons in a candidate $Z \rightarrow e^+e^-$ event will not belong to the same category. In this case, it is difficult to know what correction factor needs to be applied to the energy of each electron in order to obtain the correct invariant mass distribution. However when both electrons in the candidate event belong to the same η and R_9 category, the correction as a function of energy for both electrons can be assumed to be the same. One can therefore look at the MC invariant mass distribution in that category, compare it the invariant mass distribution of the corresponding candidate events in data, and infer the energy-dependent correction to be applied to electrons in the category in order to retrieve the required distribution. In this way, $Z \rightarrow e^+e^-$ events with both leptons in the same category allow the calculation of the required correction to be applied to *individual* electrons in that category (and crucially, regardless of the category of the other lepton in the corresponding event). Once this procedure has been followed for all categories, the events where the electrons belong to different categories can also be corrected (since each one will belong to a category where the required correction for an individual electron is known). The result will be a set of corrections to apply in any η, R_9 scenario, thus providing the calibration. This is known as the “smearing method”.

Apart from actual calibration, the **ECALELF** tool can be used to run general studies on ECAL performance using the output data from the step before the application of the smearing method. Namely, one can theoretically compare the **ECALELF ROOT ntuples** (FIXME cite) resulting from different CMSSW releases, since the **ntuples** will be in the same format.

Although **ECALELF** provides an opportunity to test the performance of the new clustering method, work needed to be done in order to make the software work in the new 70X environment. Various variables had changed from one version to the other, so an update was needed. In order to run a proper comparison, a version of **ECALELF** which functioned within both 53X and 70X was needed. In other words, we needed to develop code which could actively detect which CMSSW version was being used, and make the required substitutions at compile time. I carried out this work and completed it in the first quarter of 2014. The rest of this chapter shows the initial results of the validation.

5.3 CMSSW_7_0_X and CMSSW_5_3_X electron matching

As mentioned previously, the output of **ECALELF** provides a good starting point to compare the performances of 70X and 53X in reconstructing ECAL objects. Although it deals with $Z \rightarrow e^+e^-$ events, the calibration can also be applied to photons by reconstructing them electrons, or using photons from the electron showers. The advantage of using **ECALELF ntuples** is also that the output from both reconstructed datasets is in an identical format.

Ideally, both MC and data from both CMSSW versions would be available, to run the **ECALELF** tool fully, and work out the best set of corrections to be applied in each case. A re-reconstruction of the full 2012 run I dataset using the 70X framework was completed in April 2014. However, at the present time, the MC for 70X is not yet available, so preliminary studies are limited to comparing data in 53X and data in 70X. The objective will be to run a deeper validation once all the required samples become available.

In the meantime, since the data samples processed with 70X and 53X represented the same underlying raw events, there was an opportunity to compare some basic quantities electron by electron. The idea was to match electrons between samples, and thereby to be able to plot distributions of the fractional changes and differences between the quantities in each of the two frameworks. The obvious way of finding matches was to use a geometrical method, requiring the moduli of $\Delta\eta$ and $\Delta\phi$ (with $\Delta X = X_{70X} - X_{53X}$) to both simultaneously be less than some threshold, which was chosen to be 0.05. In addition, such a property was required to hold for **both** electrons in the $Z \rightarrow e^+e^-$ event, when comparing to a candidate event in the alternative framework. Only then could a match be declared.

The first step, however was to amend **ECALELF** to produce such a map. Part of my work was to write the algorithm which would match the electrons in one sample with the electrons in the other. The difficulty was that electrons might not be reconstructed in the same order depending on the framework: so for each entry in the first sample, all of the entries in the second sample needed to be scanned for candidates. Given the large number of electrons in any of the run I samples, a consideration was to ensure that running such a program did not take an unreasonable amount of time. To speed up the

process, the fact that the `runNumber` and `eventNumber` of corresponding electrons in each sample should match was employed. Another trick was to store a list of all allowed candidate entries in a `std::vector`, and then to remove candidates entries in case of a match. That way, the next iteration would not need to scan over events which had already been assigned. Originally, a simple entry-by-entry rejection of candidates which did not have a matching `eventNumber` and `runNumber` was used, however this version of the programme took $> 10\text{h}$ to process one of the subsamples. A modification was introduced, which used a new user-defined class comprising of `eventNumber` and `runNumber` and a `std::multimap` class (which replaced the `vector` in the previous version). The `std::multimap` class is useful because it allows elements to be mapped to a “key”. If multiple entries have the same key, the class can return a range of entries which can be iterated over. In our case, the new class comprising of ordered `eventNumber` and `runNumber` pairs was used as the key for the `std::multimap` of candidate entries, allowing the iteration over relevant entries only, rather than iteration over all entries with case-by-case rejection of those with the wrong `eventNumber` and `runNumber`. With this new method, the matching of one subsample took around 10min, and found matches for $\sim 80\%$ of electrons. (FIXME provide explanation as to why the other 20% didn’t get matched). The programme was also able to tell if the order of electrons within an entry was switched, and record this information for use later. The information was recorded in a new `TTree`: for every entry in one tree, the number of the corresponding entry in the second tree, and whether the order of electrons within a pair had been reversed. If no match was found, the matching entry in the second `TTree` was recorded as -1 .

5.4 Initial validation work

With the two data samples and the dictionary `TTree` linking them, it was possible to begin comparing quantities from one framework to another. Some of the basic quantities which I was asked to compare for the two were: the reconstructed electron Energy, the electron R_9 , the reconstructed electron track and supercluster η, ϕ coordinates, the ratio E/p , the fraction of energy emitted in bremsstrahlung and the invariant mass distribution of the $Z \rightarrow e^+e^-$ system.

5.4.1 Energy

The reconstruction of the energy of ECAL objects is clearly of paramount interest in this study. Fig. 9 shows the fractional energy difference $(E_{70X} - E_{53X})/E_{53X}$ for two different estimations of energy: the raw energy (Fig. 9a and 9b), which is simply the sum of the energies in the crystals forming the supercluster, and the corrected energy (Fig. 9c and 9d), which is the “best estimate” using the most sophisticated regression available for each model. In the latter case, the corrected energy for 53X is the “best” option available, while the corrected energy for 70X is simply an initial attempt at correction, which is likely to improve greatly once the the sample is calibrated using the MC. The figures indicate that the average change between the corrected energies in the EB is of the order of $\sim 0.12\%$, and in the EE of the order of $\sim 0.3\%$. However, this is only a preliminary result and needs to be further examined. For instance, it needs to be understood whether the “corrected’ energies” used actually provide a fair comparison, as this is far from being the best possible estimate for 70X.

5.4.2 E/p

The quantity E/p is important to check because it is used as a direct input into one of the calibration modules. Fig. 10a shows the distributions of E/p for all electrons in the sample for each framework: the red histogram represents the distribution in the 53X framework, while the blue histogram represents the distribution in the 70X framework. Only electrons which were matched in both samples were used for these plots. Fig. 10b represents the difference between these two quantities. FIXME why is this important?

5.4.3 R_9

For electrons, the interpretation of R_9 is different to that for photons. In this case, it indicates whether an electron is likely to have emitted a large fraction of its energy through bremsstrahlung or not. electrons with $R_9 > 0.94$ are likely to have lost little. On the other hand, electrons with $R_9 \leq 0.94$ will have little more of their energy before hitting the detector. In this case, they are more difficult to reconstruct. Fig. 11a shows the distribution of the R_9 of electrons in the data samples. The red line refers to

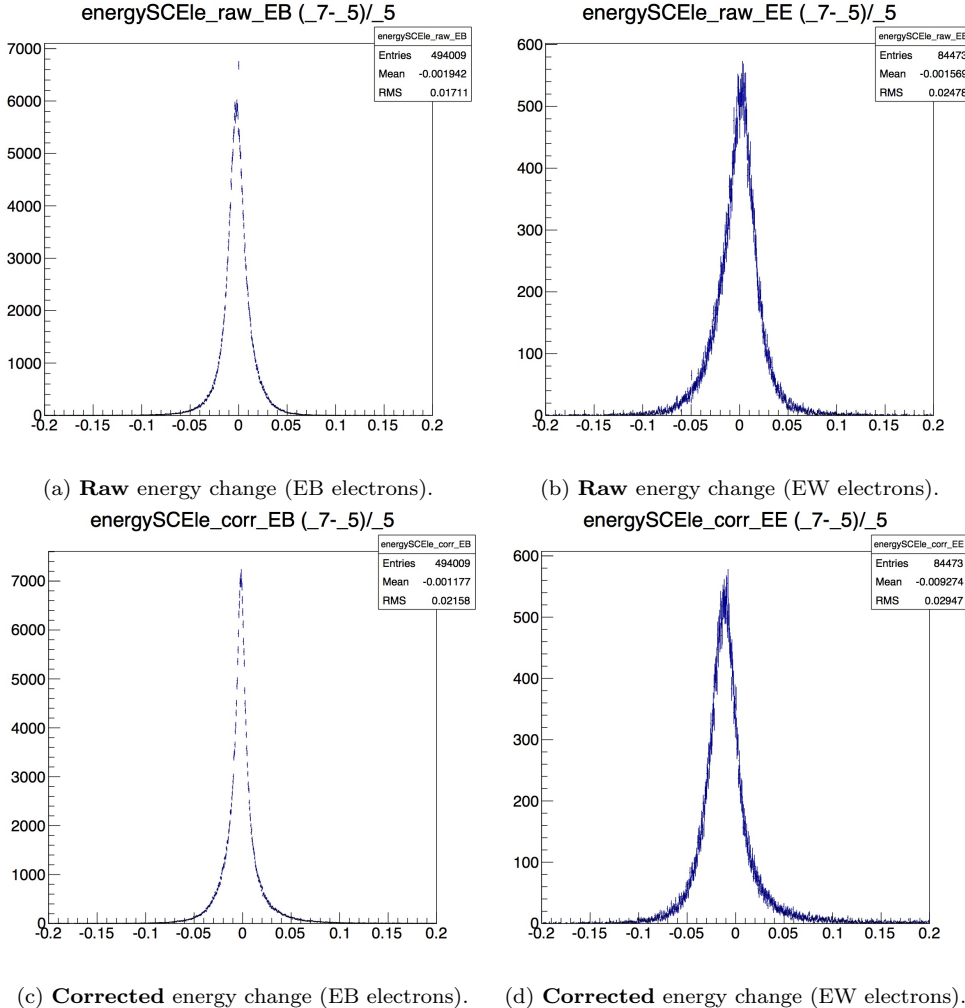


Figure 9: Fractional energy difference $\frac{E_{70X} - E_{53X}}{E_{53X}}$ for electrons in the ECAL barrel (EB) and endcaps (EE) for two versions of reconstructed energy (raw supercluster energy, and corrected supercluster energy).

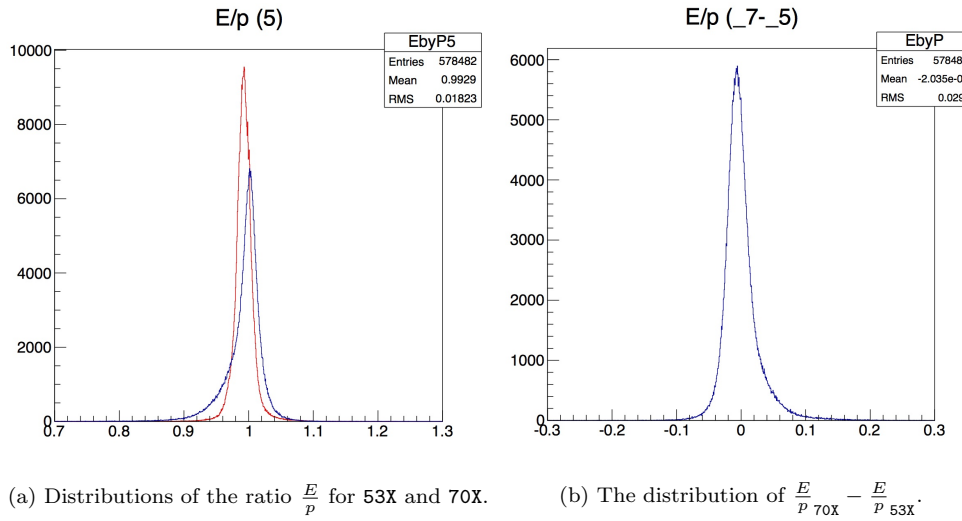


Figure 10: $\frac{E}{p}$ is calculated using the corrected energy.

electrons reconstructed in 53X, while the blue line shows the distributions of electrons reconstructed in

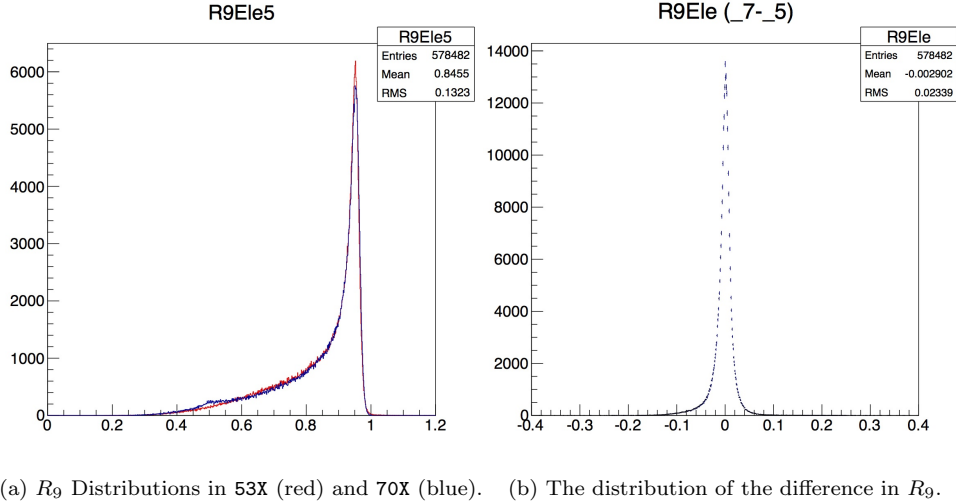


Figure 11: R_9 validation plots.

70X. Only electrons which had a match from one sample to the other were included. The distributions match up well, apart from the peak, where the 70X distribution is not as high, and around 0.5, where the 70X distribution shows a bump. These features need to be investigated further. Fig. 11b shows the distribution of the difference in R_9 (ie $(R_9)_{70X} - (R_9)_{53X}$). This forms a tight peak around 0, indicative that the two versions are generally assigning the same value of R_9 to the electrons.

5.4.4 Bremmstrahlung fraction

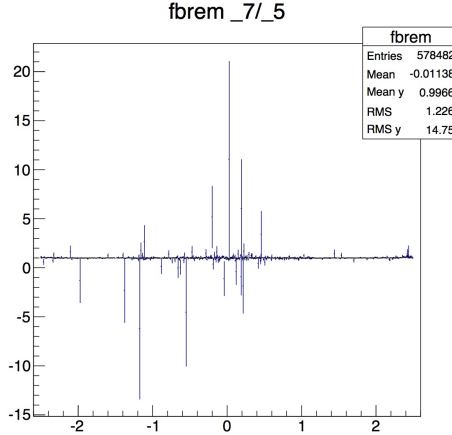


Figure 12: Ratio of bremmstrahlung fractions versus η .

A related object is the bremmstrahlung fraction f_{brem} , defined $(p_{\text{in}} - p_{\text{out}})/p_{\text{in}}$ (where p is the electron 4-momentum and the subscripts “in” and “out” refer to whether the momentum is measured as the electron leaves or enters the tracker (FIXME check!!)). In theory, this quantity should not change between 70X and 53X, and indeed Fig. 12 shows that the ratio of the f_{brem} in 53X and 70X is consistent with 1 across all of η .

5.4.5 η, ϕ coordinates

The position where the electrons hit the ECAL (known as the supercluster position $\eta_{\text{SC}}, \phi_{\text{SC}}$) should not be largely affected by the change in framework, and neither should the coordinates of the electron tracks (in this case, known as η, ϕ (the difference between the two is that $\eta_{\text{SC}}, \phi_{\text{SC}}$ are measured from the centre of the detector, while η, ϕ start at the interaction vertex, and thus are shifted in the z -direction). Fig.

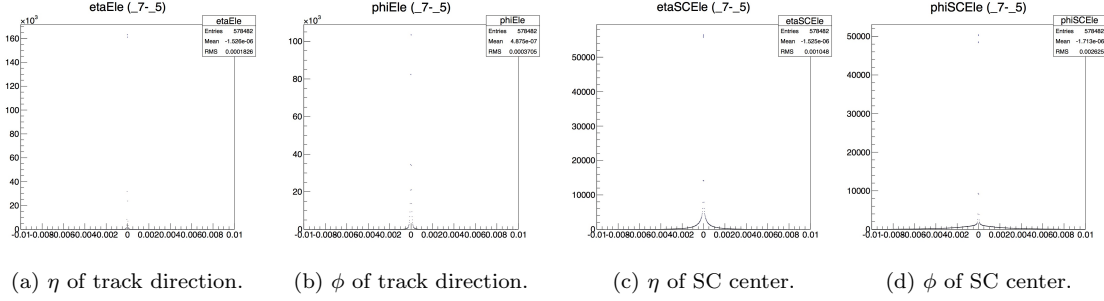


Figure 13: The distributions of $\Delta\eta, \Delta\phi$ for tracks and superclusters.

?? shows the distributions of the change in the value of $\eta_{SC}, \phi_{SC}, \eta$ and ϕ . As expected, the distributions form extremely narrow peaks around zero. This indicates that indeed, the values of the coordinates remain largely unaffected. The values of η_{SC}, ϕ_{SC} are more affected than η, ϕ , but this makes sense, since η_{SC}, ϕ_{SC} are the coordinates of the most energetic crystal in the cluster, and thus would be more affected by a change in clustering algorithm.

5.4.6 $Z \rightarrow e^+e^-$ invariant mass

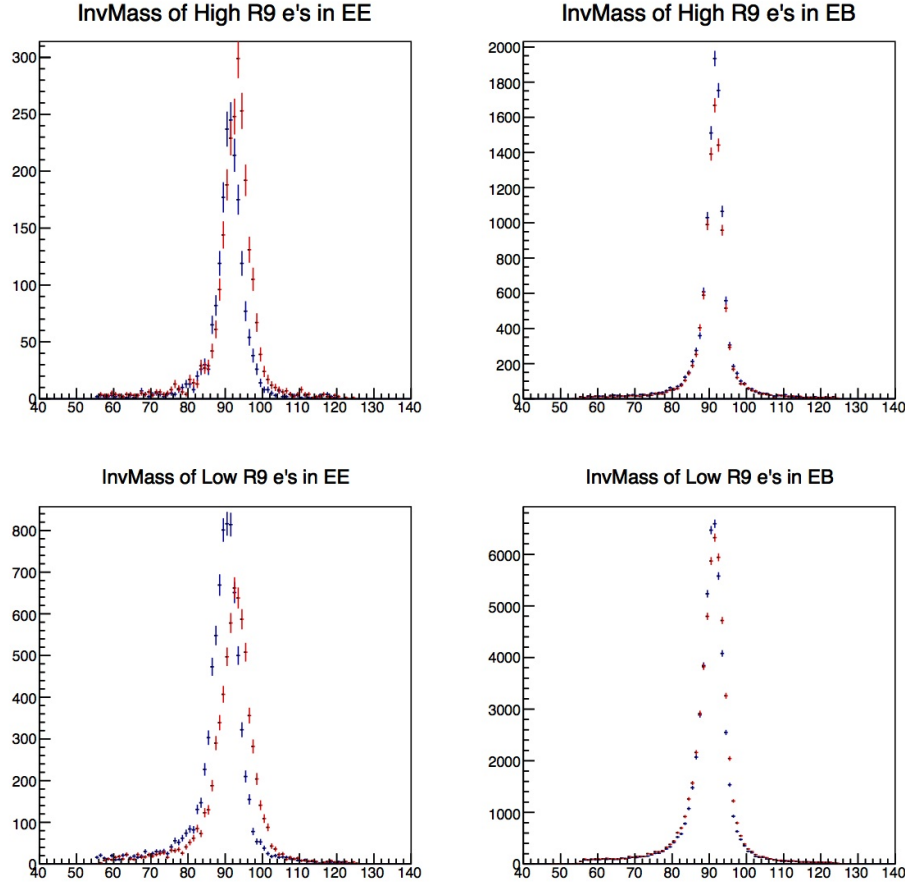


Figure 14: Invariant mass distributions of $Z \rightarrow e^+e^-$ systems when both electrons are in the same $|\eta|, R_9$ category. The red histogram indicates 53X while the blue histogram indicates 70X.

Finally, the invariant mass distributions of various categories of $Z \rightarrow e^+e^-$ system are shown. There are four categories considered here: a) both resulting electrons have $R_9 > 0.94$ and are both in the

EE, b) both with $R_9 > 0.94$ and in the EB, c) both with $R_9 \leq 0.94$ and in EE and d) c) both with $R_9 \leq 0.94$ and in EB. The red lines indicate the distributions obtained when considering electrons in the 53X frameworks, while the blue lines represent electrons from the 70X version. Only matched electrons are included in this plot. The Invariant mass is calculated using the corrected energy of the electrons - the best available for both 70X and 53X. The plots show good agreement in the two EB categories, where the two peaks overlap well, apart from the height of the peak. There is however a visible discrepancy in the EE, the the peaks appear shifted with respect to one another. Further investigation is needed to understand the differences observed.

5.5 Next Steps

This section has shown results from the preliminary steps of validation of the regression in the 70X framework. At the moment, the comparisons are being made using data reconstructed in both 53X and 70X, but for full validation, matching MC samples are needed also. Although some variables appear to match (namely the $\eta_{\text{SC}}, \phi_{\text{SC}}, \eta$ and ϕ), more studies are needed to probe differences observed between energy-based variables. The MC for the 70X sample is due to become available shortly, so we will be able to run the ECALELF tool in its entirety, and thus provide a better correction for the 70X energy. This new correction should allow a fairer comparison to be made. I am working with the ECAL DPG to pursue this work.

6 Conclusion

The $H \rightarrow \gamma\gamma$ working group are in the process of finalising the legacy analysis for the $\sqrt{s} = 7$ and 8 TeV data samples from run I. This will include a mass measurement for the Higgs boson based on a similar analysis to the one described above. An analysis of the spin properties of this particle, which I was involved in, will also be included. This publication will reflect the final word on the older data samples from the perspective of the CMS $H \rightarrow \gamma\gamma$ analysis. The LHC should begin colliding again in 2015, and new data will then become available. Various new measurements will need to be made to further understand the properties of the Higgs boson. Further data will be able to shed light on the existence of a potential second Higgs boson (multiple such bosons are predicted in various BSM frameworks), and will allow precision measurements of differential cross sections, couplings and spin/parity. Deviations from the expected properties of the SM Higgs boson could signal the potential existence of BSM physics. $H \rightarrow \gamma\gamma$ will remain one of the most sensitive channels with which to analyse the properties of the Higgs during run II. On a more personal note, my work within the CMS experiment will initially be centred around the ECAL, preparing for calibration in run II. The way that photons are reconstructed is being modified, and I will help determine what the effect of this change will be on the sensitivity of the $H \rightarrow \gamma\gamma$ analysis. As 2015 approaches, I will become involved in planning and implementing the next round of analysis, to help further pin down the properties of the Higgs boson. To conclude, it is clear that even though we have now discovered the elusive Higgs boson, many questions remain unanswered. In 2015, some BSM theories which might help to answer these questions will be tested. If nothing is found in direct searches, the precision analysis of the properties of the Higgs boson will be one of key avenues with which to search for deviations from the SM. As such, further understanding of the Higgs boson's properties are not only desirable, but indeed imperative if we are to understand more about the fundamental structure of the universe.

References

- [1] J. E. Augustin et al. Discovery of a Narrow Resonance in e^+e^- Annihilation. *Phys. Rev. Lett.*, 33:1406–1408, Dec 1974.
- [2] J. J. Aubert et al. Experimental Observation of a Heavy Particle *J. Phys. Rev. Lett.*, 33:1404–1406, Dec 1974.
- [3] S. L. Glashow, J. Iliopoulos, and L. Maiani. Weak Interactions with Lepton-Hadron Symmetry. *Phys. Rev.*, D2:1285–1292, Oct 1970.
- [4] A. Salam. Weak and Electromagnetic Interactions. *Conf. Proc.*, C680519:367–377, 1968.

- [5] S. Weinberg. A Model of Leptons. *Phys. Rev. Lett.*, 19:1264–1266, Nov 1967.
- [6] F. Englert and R. Brout. Broken symmetry and the mass of gauge vector mesons. *Phys. Rev. Lett.*, 13:321–323, Aug 1964.
- [7] P. W. Higgs. Broken symmetries, massless particles and gauge fields. *Phys. Lett.*, 12:132–133, September 1964.
- [8] P. W. Higgs. Broken symmetries and the masses of gauge bosons. *Phys. Rev. Lett.*, 13:508–509, Oct 1964.
- [9] G. S. Guralnik, C. R. Hagen, and T. W. B. Kibble. Global conservation laws and massless particles. *Phys. Rev. Lett.*, 13:585–587, Nov 1964.
- [10] P. W. Higgs. Spontaneous symmetry breakdown without massless bosons. *Phys. Rev.*, 145:1156–1163, May 1966.
- [11] T. W. B. Kibble. Symmetry breaking in non-abelian gauge theories. *Phys. Rev.*, 155:1554–1561, Mar 1967.
- [12] M. L. Perl et al. Evidence for anomalous lepton production in $e^+ e^-$ annihilation. *Phys. Rev. Lett.*, 35:1489–1492, 1975.
- [13] S. W. Herb et al. Observation of a dimuon resonance at 9.5-GeV in 400-GeV proton - nucleus collisions. *Phys. Rev. Lett.*, 39:252–255, 1977.
- [14] R. Brandelik et al. Evidence for planar events in e^+e^- annihilation at high energies. *Phys. Lett. B*, 86:243–249, September 1979.
- [15] D. P. Barber et al. Discovery of Three-Jet Events and a Test of Quantum Chromodynamics at PETRA. *Phys. Rev. Lett.*, 43:830–833, September 1979.
- [16] C. Berger et al. Evidence for gluon bremsstrahlung in e^+e^- annihilations at high energies. *Phys. Lett. B*, 86:418–425, October 1979.
- [17] G. Arnison et al. Experimental observation of lepton pairs of invariant mass around 95 GeV at the CERN SPS collider. *Phys. Lett.*, B126:398–410, 1983.
- [18] M. Banner et al. Observation of single isolated electrons of high transverse momentum in events with missing transverse energy at the CERN $\bar{p} - p$ collider. *Phys. Lett.*, B122:476–485, 1983.
- [19] F. Abe et al. Observation of top quark production in anti-p p collisions. *Phys. Rev. Lett.*, 74:2626–2631, 1995.
- [20] S. Abachi et al. Observation of the top quark. *Phys. Rev. Lett.*, 74:2632–2637, 1995.
- [21] K. Kodama et al. Observation of tau neutrino interactions. *Phys. Lett.*, B504:218–224, 2001.
- [22] S. Chatrchyan et al. Observation of a new boson at a mass of 125 GeV with the CMS experiment at the LHC. *Phys. Lett.*, B716:30–61, 2012.
- [23] G. Aad et al. Observation of a new particle in the search for the Standard Model Higgs boson with the ATLAS detector at the LHC. *Phys. Lett.*, B716:1–29, 2012.
- [24] Y. Fukuda, T. Hayakawa, E. Ichihara, et al. Evidence for Oscillation of Atmospheric Neutrinos. *Phys. Rev. Lett.*, 81:1562–1567, August 1998.
- [25] Q. R. Ahmad, R. C. Allen, T. C. Andersen, et al. Measurement of the Rate of $\nu_e + d \rightarrow p + p + e^-$ Interactions Produced by ${}^8\text{B}$ Solar Neutrinos at the Sudbury Neutrino Observatory. *Phys. Rev. Lett.*, 87(7):071301, August 2001.
- [26] F. P. An, J. Z. Bai, A. B. Balantekin, et al. Observation of Electron-Antineutrino Disappearance at Daya Bay. *Phys. Rev. Lett.*, 108(17):171803, April 2012.

- [27] P. A. R. Ade, N. Aghanim, C. Armitage-Caplan, et al. Planck 2013 results. I. Overview of products and scientific results. (arXiv:1303.5062), March 2013.
- [28] S. P. Martin. A Supersymmetry primer. *Kane, G.L. (ed.): Perspectives on supersymmetry II*, (arXiv:hep-ph/9709356), 1997.
- [29] U. Sarkar. Particle and astroparticle physics. *Taylor and Francis*, 2008.
- [30] S. Dittmaier et al. Handbook of LHC Higgs Cross Sections: 1. Inclusive Observables. (arXiv:1101.0593. CERN-2011-002), 2011.
- [31] S. Dittmaier et al. Handbook of LHC Higgs Cross Sections: 2. Differential Distributions. (arXiv:1201.3084. CERN-2012-002), 2012.
- [32] S. Heinemeyer, C. Mariotti, G. Passarino, et al. Handbook of LHC Higgs Cross Sections: 3. Higgs Properties. (arXiv:1307.1347. CERN-2013-004), 2013. Comments: 404 pages, 139 figures, to be submitted to CERN Report. Working Group web page: <https://twiki.cern.ch/twiki/bin/view/LHCPhysics/CrossSections>.
- [33] G. L. Bayatian et al. CMS Physics: Technical Design Report Volume 1: Detector Performance and Software. 2006.
- [34] *The CMS electromagnetic calorimeter project: Technical Design Report*. Technical Design Report CMS. CERN, Geneva, 1997.
- [35] S. Chatrchyan et al. The CMS experiment at the CERN LHC. *JINST*, 3:S08004, 2008.
- [36] Federico De Guio. Performance of the CMS electromagnetic calorimeter and its role in the hunt for the Higgs boson in the two-photon channel. *J.Phys.Conf.Ser.*, 455:012028, 2013.
- [37] V Karimäki, M Mannelli, P Siegrist, H Breuker, A Caner, R Castaldi, K Freudenreich, G Hall, R Horisberger, M Huhtinen, and A Cattai. *The CMS tracker system project: Technical Design Report*. Technical Design Report CMS. CERN, Geneva, 1997.
- [38] *The CMS hadron calorimeter project: Technical Design Report*. Technical Design Report CMS. CERN, Geneva, 1997.
- [39] *The CMS muon project: Technical Design Report*. Technical Design Report CMS. CERN, Geneva, 1997.
- [40] C. J. Seez et al. Photon decay modes of the intermediate mass Higgs. *Conf. Proc.*, C901004:474–487, 1990.
- [41] S. Chatrchyan et al. Observation of a new boson with mass near 125 GeV in pp collisions at $\sqrt{s} = 7$ and 8 TeV. *JHEP*, 06:081, 2013.
- [42] Byron P. Roe, Hai-Jun Yang, Ji Zhu, Yong Liu, Ion Stancu, and Gordon McGregor. Boosted decision trees as an alternative to artificial neural networks for particle identification. *Nuclear Instruments and Methods in Physics Research Section A: Accelerators, Spectrometers, Detectors and Associated Equipment*, 543(2–3):577 – 584, 2005.
- [43] S Chatrchyan et al. Search for the standard model Higgs boson decaying into two photons in pp collisions at $\sqrt{s} = 7$ TeV. *Phys. Lett.*, B710:403–425, 2012.
- [44] G. L. Bayatian, S. Chatrchyan, G. Hmayakyan, et al. *CMS Physics: Technical Design Report Volume 1: Detector Performance and Software*. Technical Design Report CMS. CERN, Geneva, 2006.
- [45] M. Anderson et al. A Review of clustering algorithms and energy corrections in the Electromagnetic Calorimeter. *CERN*, CMS Internal Note, 2010/008.
- [46] CMS Collaboration. Particle–Flow Event Reconstruction in CMS and Performance for Jets, Taus, and MET. *CERN*, CMS Physics Analysis Summary, PFT-09-001.